AAAS
Research
Volume 2020, Article ID 9426453, 15 pages
https://doi.org/10.34133/2020/9426453

Research
A SCIENCE PARTNER JOURNAL

Research Article

Biofilm Microenvironment-Responsive Nanotheranostics for Dual-Mode Imaging and Hypoxia-Relief-Enhanced Photodynamic Therapy of Bacterial Infections

Weijun Xiu,[1] Siyu Gan,[1] Qirui Wen,[1] Qiu Qiu,[1] Sulai Dai,[1] Heng Dong,[2] Qiang Li,[2] Lihui Yuwen,[1] Lixing Weng,[3] Zhaogang Teng,[4] Yongbin Mou,[2] and Lianhui Wang[1]

[1]*Key Laboratory for Organic Electronics and Information Displays & Jiangsu Key Laboratory for Biosensors, Institute of Advanced Materials (IAM), Jiangsu National Synergetic Innovation Centre for Advanced Materials (SICAM), Nanjing University of Posts and Telecommunications, Nanjing 210023, China*
[2]*Department of Oral Implantology, Nanjing Stomatological Hospital, School of Medicine, Nanjing University, Nanjing 210023, China*
[3]*School of Geography and Biological Information, Nanjing University of Posts and Telecommunications, Nanjing 210023, China*
[4]*Department of Medical Imaging, Jinling Hospital, School of Medicine, Nanjing University, Nanjing 210002, China*

Correspondence should be addressed to Lihui Yuwen; iamlhyuwen@njupt.edu.cn and Lianhui Wang; iamlhwang@njupt.edu.cn

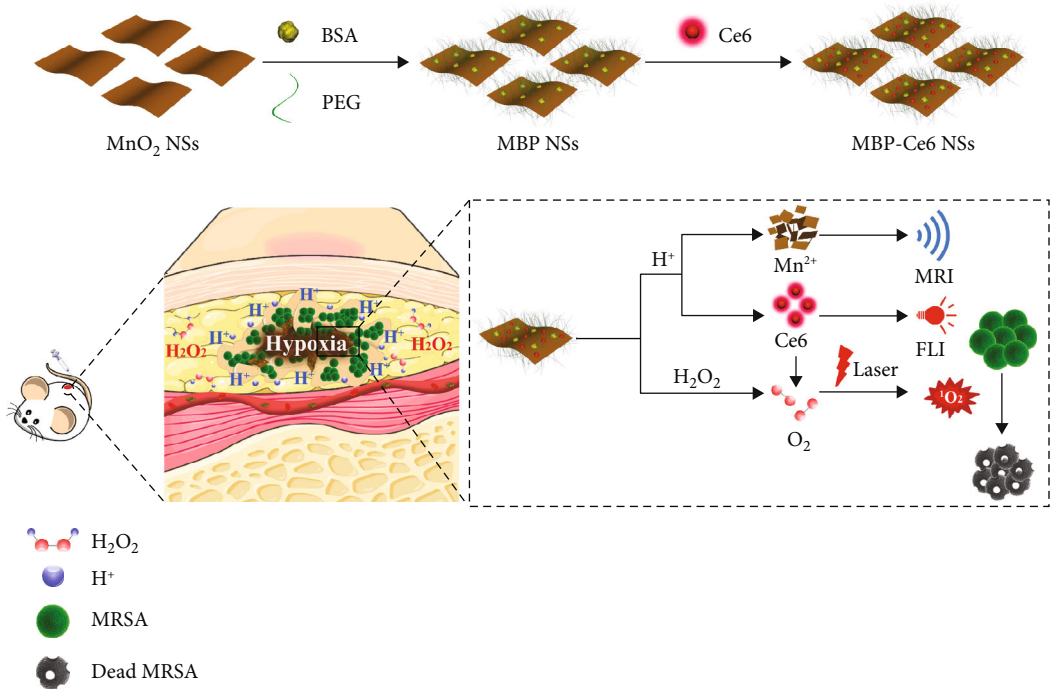
Received 10 January 2020; Accepted 5 March 2020; Published 24 March 2020

Copyright © 2020 Weijun Xiu et al. Exclusive Licensee Science and Technology Review Publishing House. Distributed under a Creative Commons Attribution License (CC BY 4.0).

The formation of bacterial biofilms closely associates with infectious diseases. Until now, precise diagnosis and effective treatment of bacterial biofilm infections are still in great need. Herein, a novel multifunctional theranostic nanoplatform based on MnO_2 nanosheets (MnO_2 NSs) has been designed to achieve pH-responsive dual-mode imaging and hypoxia-relief-enhanced antimicrobial photodynamic therapy (aPDT) of bacterial biofilm infections. In this study, MnO_2 NSs were modified with bovine serum albumin (BSA) and polyethylene glycol (PEG) and then loaded with chlorin e6 (Ce6) as photosensitizer to form MnO_2-BSA/PEG-Ce6 nanosheets (MBP-Ce6 NSs). After being delivered into the bacterial biofilm-infected tissues, the MBP-Ce6 NSs could be decomposed in acidic biofilm microenvironment and release Ce6 with Mn^{2+}, which subsequently activate both fluorescence (FL) and magnetic resonance (MR) signals for effective dual-mode FL/MR imaging of bacterial biofilm infections. Meanwhile, MnO_2 could catalyze the decomposing of H_2O_2 in biofilm-infected tissues into O_2 and relieve the hypoxic condition of biofilm, which significantly enhances the efficacy of aPDT. An *in vitro* study showed that MBP-Ce6 NSs could significantly reduce the number of methicillin-resistant *Staphylococcus aureus* (MRSA) in biofilms after 635 nm laser irradiation. Guided by FL/MR imaging, MRSA biofilm-infected mice can be efficiently treated by MBP-Ce6 NSs-based aPDT. Overall, MBP-Ce6 NSs not only possess biofilm microenvironment-responsive dual-mode FL/MR imaging ability but also have significantly enhanced aPDT efficacy by relieving the hypoxia habitat of biofilm, which provides a promising theranostic nanoplatform for bacterial biofilm infections.

1. Introduction

Bacterial infection is a prominent threat for human health. Numerous bacterial infections, including dental caries, cystic fibrosis, pneumonia, otitis media, and especially chronic wounds, usually relate with the formation of bacterial biofilms [1–5]. Biofilm is the aggregated bacterial populations which are usually encapsulated in the extracellular polymeric substances (EPS) and attach to the living or inert surfaces [6, 7]. The compact EPS of bacterial biofilm not only protect themselves from the attack of host immune system but also cause serious antibiotic resistance, which bring great challenge to eradicate bacterial biofilm infections [8, 9]. Specific and sensitive diagnosis of bacterial biofilm infections is essential to effectively treat these diseases [10–12]. Traditional diagnostic methods, such as culture method, biochemistry identification, and polymerase chain reaction (PCR), have been widely used in bacterial biofilm infections diagnosis.However, these *ex vivo* methods generally need invasive tissue ablation, time-consuming procedures,



Scheme 1: The preparation of MnO_2-BAS/PEG-Ce6 nanosheets (MBP-Ce6 NSs) and their use for responsive FL/MR imaging and enhanced aPDT of bacterial biofilm infections.

and have low sensitivity [13–15]. Noninvasive and effective detection methods of bacterial biofilm infections *in vivo* are highly desired.

Recently, various imaging technologies have been developed for the detection of bacterial infections. Considered as a sensitive method for disease diagnosis, fluorescence imaging (FLI) has received great attention [15, 16]. Numerous bacteria-targeting fluorescent imaging probes have been designed for FLI of bacterial infections, such as maltodextrin, vancomycin, and *N*-acetylmuramic acids functionalized dyes [17–19]. Nevertheless, the light scattering and absorption in biological tissues usually cause poor penetration of FLI [20, 21]. In comparison, magnetic resonance imaging (MRI) has the advantages of deep tissue penetration and high spatial resolution [22]. Previous work has reported the use of MRI technique to monitor the bacterial infections [23]. However, relatively low sensitivity of MRI limits its application for bacterial infections [22]. Currently, most imaging probes with bacterial detection ability only work in single mode, which usually limits their use due to the intrinsic shortcomings of each imaging mode. Moreover, these imaging probes mentioned above were designed to target planktonic bacteria rather than bacterial biofilms. The dense EPS matrix of biofilm may prevent the penetration of imaging agents and limit their application for bacterial biofilm infections. In addition, currently used imaging probes for bacterial infections usually work in "always-on" mode that may cause significant background signal and reduce their sensitivity. Therefore, FL/MR dual-mode imaging probes with bacterial biofilm responsive and activable ability are very promising.

Due to the encapsulation of EPS and fermentation of bacteria inside biofilm, the biofilm microenvironment has several characteristics, such as the lack of oxygen, low pH, and high level of H_2O_2 compared with healthy tissues [24–29]. Hence, biofilm microenvironment is an ideal target for specific diagnosis and treatment of biofilm-related infection diseases [29–31]. Previous studies have demonstrated the use of charge-switchable nanozymes to respond the acidic biofilm microenvironment through bioorthogonal reaction to activate profluorophores and realize specific fluorescence detection of biofilm *in vitro* [24]. Moreover, pH-responsive Au nanoparticles and micellar nanocarriers have also been designed to combat bacterial biofilm infections [32, 33]. Although these studies are promising, they usually work in single mode (diagnosis or treatment) and lack the ability of simultaneous diagnosis and therapy. To the best of our knowledge, biofilm microenvironment-responsive nanotheranostics that combine both activable dual-mode FL/MR imaging and treatment abilities to combat biofilm infections are rarely reported.

Here, we designed a biofilm microenvironment-responsive theranostic nanoagent (MBP-Ce6 NSs) for dual-mode FL/MR imaging and enhanced aPDT of MRSA biofilm infections. As Scheme 1 shows, MnO_2 nanosheets (MnO_2 NSs) were modified with biocompatible BSA and PEG to form MnO_2-BSA/PEG NSs (MBP NSs). Then, a photosensitizer Ce6 was further loaded to prepare MBP-Ce6 NSs. The fluorescence of Ce6 could be quenched after loading on the surface of MnO_2 NSs. In acidic biofilm microenvironment, MnO_2 NSs were decomposed and generate Mn^{2+} ions, which can be used for biofilm responsive T_1-weighted MRI [21, 33, 34]. Meanwhile, the decomposition of MnO_2 will also result in the release of Ce6 from the MBP-Ce6 NSs, restoration of the fluorescence of Ce6, and realization of

the biofilm-activable fluorescence imaging. Moreover, the released Ce6 can also serve as the photosensitizer for aPDT and generate singlet oxygen ($^1O_2$) under light irradiation. $^1O_2$ can effectively damage the vital biomacromolecules (DNA, protein, etc.) and has been used for the treatment of cancer and bacterial infection [28, 34, 35]. Since it is difficult for bacteria to develop resistance to $^1O_2$, aPDT is regarded as an effective approach for the drug-resistant bacterial infection [32, 36]. However, the therapeutic efficacy of aPDT would be restricted by hypoxia condition in biofilm-infected tissues [4, 26]. Due to the high level H_2O_2 in biofilm-infected tissues, MnO_2 NSs can convert the H_2O_2 into O_2 and enhance O_2-dependent aPDT. MBP-Ce6 NSs were successfully used for acid-activated dual-mode imaging and hypoxia relieving aPDT of MRSA biofilm-infected mice.

2. Results and Discussion

2.1. Material Preparation and Characterization. MnO_2 NSs were synthesized according to the reported method [37]. Manganese (II) chloride reacted with H_2O_2 and tetramethylammonium hydroxide (TMA·OH) to form aggregated MnO_2 NSs (Figure S1, Supporting Information). MnO_2 NSs were prepared by ultrasonication-assisted exfoliation of the as-prepared MnO_2 NSs and followed by gradient centrifugation. Transmission electron microscopy (TEM) images (Figure 1(a); Figures S2(a) and (d), Supporting Information) show that the as-prepared MnO_2 NSs have uniform sheet-like morphology and small average size (<100 nm). As the selected area electron diffraction (SAED) pattern (Figure S3(a), Supporting Information) shows, MnO_2 NSs have a polycrystalline structure. A high-resolution TEM (HRTEM) image (Figure 1(b)) shows the distinct crystal lattice spacing about 0.21 nm, which can be ascribed to the (202) plane of MnO_2 [20, 37]. A high-angle annular dark-field scanning transmission electron microscopy (HAADF-STEM) image and energy dispersive spectroscopy (EDS) elemental mapping images (Figures S3(b), (c), (d), and (e), Supporting Information) show homogeneous element distribution in MnO_2 NSs. Atomic force microscopy (AFM) images (Figure 1(c); Figures S4(a) and (d), Supporting Information) reveal that the average thickness of MnO_2 NSs is about 1.08 nm, which proves the single-layer structure of MnO_2 NSs [37]. To enhance the stability and biocompatibility of MnO_2 NSs, BSA and PEG_{3000}-NH_2 were used to modify the surface of MnO_2 NSs through the van der Waals interaction and Mn-N coordinate bonding to form MBP NSs [20, 38]. Next, Ce6 was further loaded on the surface of MBP NSs by similar noncovalent interactions [39]. As the TEM images (Figure 1(e) and (i); Figures S2(b), (c), (e), and (f), Supporting Information) and HRTEM images (Figure 1(f) and (j)) show, the morphology, size, and crystal structure of the MBP NSs and MBP-Ce6 NSs have no obvious change compared with MnO_2 NSs. The thickness of MBP NSs increased to about 5.07 nm (Figure 1(g) and (h); Figures S4(b) and (e), Supporting Information) due to the existence of BSA and PEG. After loading with Ce6, the thickness of MBP-Ce6 NSs further increased to about 5.36 nm (Figure 1(k) and (l); Figures S4(c) and (f), Supporting Information).

The crystal structure of MnO_2 NSs was determined by X-ray diffraction (XRD). Based on the XRD pattern of MnO_2 NSs shown in Figure 1(m), three diffraction peaks, located at 8.7°, 18.8°, and 37.0°, can be assigned to the (001), (002), and (100) planes, respectively [37]. The Fourier transform infrared spectroscopy (FT-IR) and X-ray photoelectron spectroscopy (XPS) were also carried out to further investigate the compositions of MBP-Ce6 NSs. As shown in Figure 1(n), the IR absorption bands of MnO_2 NSs around 500 cm^{-1} belong to the Mn-O stretching vibrations [37]. The IR absorption bands of MBP NSs at 2926 cm^{-1} and 2855 cm^{-1} can be ascribed to the C-H stretching vibrations from the PEG [40]. The IR adsorption bands of MBP-Ce6 NSs near 1650 cm^{-1} and 1590 cm^{-1} can be assigned to the C=O bending vibrations from BSA and the N-H bending vibrations from Ce6, respectively [40, 41]. The XPS survey spectrum (Figure 1(o)) of MnO_2 NSs shows the binding energy peaks located at 654 eV and 642 eV, which belong to Mn (IV) $2p_{1/2}$ and Mn (IV) $2p_{3/2}$ of MnO_2 [42]. For the MBP-Ce6 NSs, the intensity of Mn 2p peaks decreases, while the intensity of N 1s (400 eV) and C 1s (285 eV) peaks increases, indicating the presence of BSA, PEG, and Ce6 on the surface of MnO_2 NSs. As Figure S5(a) (Supporting Information) shows, the hydrodynamic diameter of MBP-Ce6 NSs is larger than that of MnO_2 and MBP NSs, suggesting the successful surface modification. The zeta potential of MnO_2 NSs is about -7.62 mV (Figure S5b, Supporting Information) [37]. After surface modification with BSA and PEG, it increased to -2.05 mV because of the existence of electroneutral PEG. While further loaded with Ce6, the zeta potential of MBP-Ce6 NSs decreased to about -35.70 mV owing to the negative charge of Ce6 [41].

Ce6 loading and fluorescence quenching abilities of MBP NSs were also investigated. As shown in Figure 2(a), the fluorescence intensity of Ce6 (20 μg/mL) nearly diminished after being mixed with MBP NSs (MnO_2: 48 μg/mL) due to the quenching of MnO_2 NS [43, 44]. The ultraviolet-visible-near infrared (UV-Vis-NIR) absorption spectrum (Figure 2(b)) of MBP-Ce6 NSs shows that the absorbance of the characteristic peaks for Ce6 near 400 and 650 nm is much higher than that of MBP NSs and MnO_2 NSs, suggesting the successful loading of Ce6 on MBP NSs [45]. As illustrated in Figure 2(c), the loading efficiency of Ce6 reaches as high as 67.5% at the feeding ratio of 6 : 1 (m_{Ce6} : m_{MBP}), while the corresponding encapsulation efficiency is about 22.5%, indicating good Ce6-loading capacity of MBP NSs.

Since MnO_2 nanostructures could be decomposed in acidic aqueous solutions and release Mn^{2+}, MnO_2 NSs have been used as pH-responsive drug delivery platforms [46]. The pH-responsive release of Ce6 by MBP-Ce6 NSs was then studied. The morphology change of MBP-Ce6 NSs after being incubated in phosphate-buffered saline (PBS) with different pH values was studied by using TEM. As shown in Figure 2(d), the MBP-Ce6 NSs gradually broke up in acidic condition (pH = 5.0) after 4 h incubation, while those in neutral PBS (pH = 7.4) still kept intact morphology even after

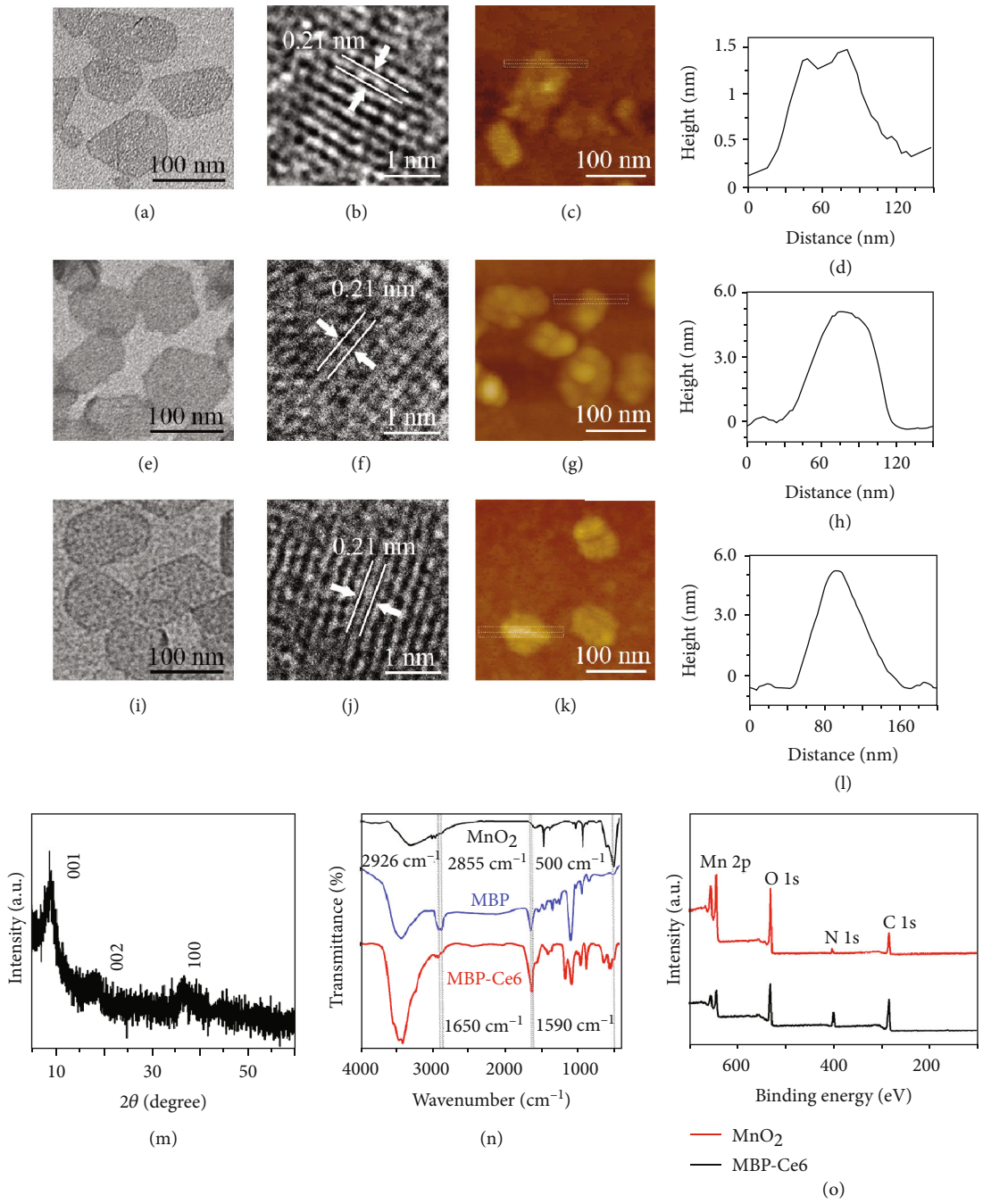


FIGURE 1: Characterization of MnO_2 NSs, MBP NSs, and MBP-Ce6 NSs. (a) TEM image, (b) HRTEM image, (c) AFM image, and (d) height profile of MnO_2 NSs. (e) TEM image, (f) HRTEM image, (g) AFM image, and (h) height profile of MBP NSs. (i) TEM image, (j) HRTEM image, (k) AFM image, and (l) height profile of MBP-Ce6 NSs. (m) XRD pattern of MnO_2 NSs. (n) FT-IR spectra of MnO_2 NSs, MBP NSs, and MBP-Ce6 NSs. (o) XPS spectra of MnO_2 NSs and MBP-Ce6 NSs.

24 h storage. The decomposition of MBP-Ce6 NSs was also studied by using the UV-Vis-NIR absorption spectroscopy. As indicated in Figure 2(e), the degradation of MBP-Ce6 NSs was less than 20% in PBS at pH = 7.4 after 24 h storage at room temperature. In comparison, nearly all the MBP-Ce6 NSs were decomposed in acidic PBS at pH = 5.0 and 6.0. The acid-induced decomposition of MBP-Ce6 NSs could trigger the fast release of Ce6. The amount of released Ce6 and the fluorescence recovery were studied by the UV-Vis-NIR absorption spectroscopy and fluorescence spectroscopy, respectively. As illustrated in Figure 2(f), the release of Ce6 is much faster in acidic conditions than in the neutral condition. In acidic PBS (pH = 5.0), the released Ce6 reached 52.64% after 24 h incubation, while that in neutral PBS (pH = 7.4) was only 18.69%. Figure S6 (Supporting Information) further indicates that the fluorescence of

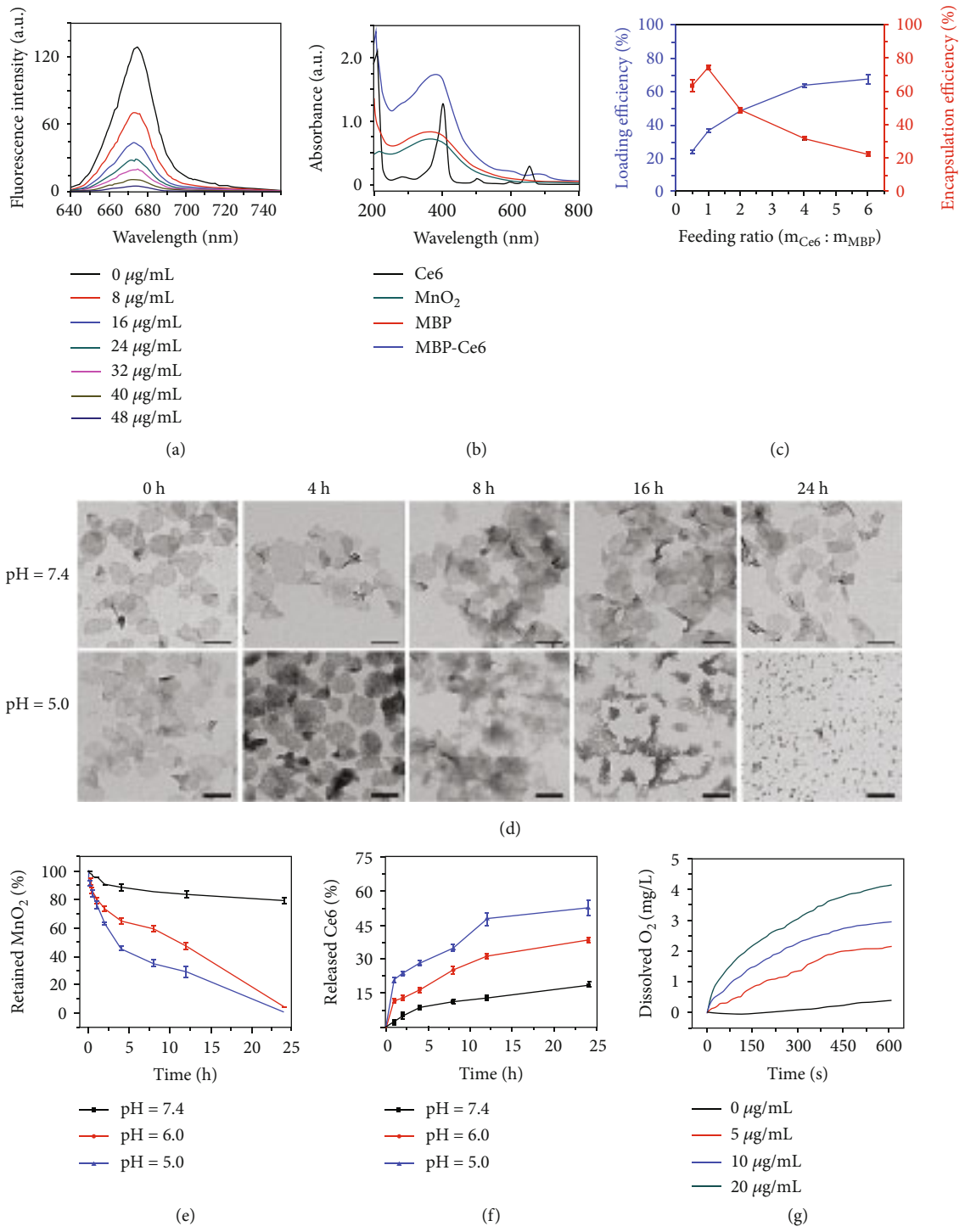


FIGURE 2: Characterization and drug release of MBP-Ce6 NSs. (a) The fluorescence spectra of Ce6 aqueous solutions (20 μg/mL) after being mixed with MnO_2 NSs (0, 6, 12, 18, 24, 30, 36, and 48 μg/mL). (b) The UV-Vis-NIR spectra of Ce6, MnO_2 NSs, MBP NSs, and MBP-Ce6 NSs. (c) The loading efficiency and encapsulation efficiency of Ce6 at different feeding ratios of Ce6 and MnO_2 NSs. (d) The TEM images of MBP-Ce6 NSs after being stored in PBS at different conditions. The scale bar is 100 nm for all TEM images. (e) The time-dependent degradation of MBP NSs (40 μg/mL) in PBS at different pH values. (f) Released Ce6 from MBP-Ce6 NSs over time at different conditions. (g) The time-dependent concentration change of dissolved O_2 in H_2O_2 solutions (50 μM) after being mixed with MBP-Ce6 NSs at different concentrations (0, 5, 10, and 20 μg/mL). Error bars indicate s.d. ($n = 3$).

Ce6 reached the highest intensity after 12 h storage, and the release of the Ce6 in acidic conditions is much faster than that in neutral condition.

Hypoxia is another typical characteristic of the microenvironment in bacterial biofilm-infected tissues [47, 48]. Since oxygen is an essential factor in the process of PDT, the

hypoxia condition can significantly limit the therapeutic efficacy of PDT. Fortunately, H_2O_2 usually exists at a relatively high level in bacteria-infected tissues and can be used as a potential oxygen source [28, 49–51]. Therefore, the peroxidase-like ability of MBP-Ce6 NSs was investigated. After MBP-Ce6 NSs were dispersed in H_2O_2 aqueous solution (50 μM), the concentration of dissolved O_2 in the mixture changed according to the concentration of MnO_2 (Figure 2(g)), which indicates that MBP-Ce6 NSs could effectively decompose H_2O_2 to release O_2. The generation of O_2 could relieve the hypoxia of bacterial biofilm-infected tissues and may further enhance the efficacy of oxygen-dependent aPDT. Therefore, the singlet oxygen ($^1O_2$) production of MBP-Ce6 NSs in hypoxic conditions with the presence of H_2O_2 was measured and evaluated by using 2′,7′-dichlorodihydrofluorescein diacetate (DCFH-DA) as the fluorescent reactive oxygen species (ROS) indicator [52–54]. As shown in Figure S7(a) (Supporting Information), the $^1O_2$ generation efficiency of MBP-Ce6 NSs is less effective than free Ce6 in normoxic condition due to the fluorescence quenching of MnO_2 NSs. In contrast, MBP-Ce6 NSs can efficiently produce high-level $^1O_2$ after laser irradiation in hypoxic conditions with the presence of H_2O_2 similar to the biofilm microenvironment, while Ce6, H_2O_2, Ce6 + H_2O_2, and MBP-Ce6 NSs generate neglectable $^1O_2$ (Figure S7(b), Supporting Information), suggesting that MBP-Ce6 NSs can serve as efficient agent during aPDT process in hypoxic conditions. These results mentioned above are consistent with the elevated concentration of O_2 shown in Figure 2(g).

The colloidal stability and cytotoxicity of MBP-Ce6 NSs were assessed before further biological applications. After being dispersed in various conditions (H_2O, PBS, and Dulbecco's modified Eagle's medium (DMEM)), MBP-Ce6 NSs showed no obvious aggregation (Figure S8(a), Supporting Information). Moreover, the change of their hydrodynamic diameters within 24 h was neglectable (Figure S8(b), Supporting Information), indicating excellent colloidal stability of MBP-Ce6 NSs. Then, MPB-Ce6 NSs with different concentrations (MnO_2: 0, 20, 40, 80, 160, and 320 μg/mL; Ce6: 0, 16, 32, 64, 128, and 256 μg/mL) were cultivated with human prostatic stromal myofibroblast (WPMY-1) cells for 24 h. Results show that MBP-Ce6 NSs have little cytotoxicity even at high concentration (Figure S9, Supporting Information).

2.2. In Vitro Photodynamic Treatment of MRSA Biofilms. To investigate the Ce6 release and fluorescence imaging abilities of MBP-Ce6 NSs in bacterial biofilms *in vitro*, MRSA biofilms were used as a model. For comparison, WPMY-1 cells were adopted as the control to mimic the normal environment condition. After being treated with MBP-Ce6 NSs (MnO_2 NSs: 100 μg/mL; Ce6: 80 μg/mL) at different times, gradually increased red fluorescence (Ce6) in MRSA biofilms could be observed from the 3D confocal laser scanning microscopy (3D CLSM) images during incubation (Figure 3(a)), while no distinct fluorescence of Ce6 could be seen for WPMY-1 cells at the same experimental conditions (Figure 3(b)). The fluorescence intensity of Ce6 incubated with MRSA biofilms is about 2.5 times higher than that of WPMY-1 cells at 12 h (Figure 3(c)), suggesting MBP-Ce6 NSs have specific biofilm microenvironment-responsive releasing ability. The size decrease of MBP-Ce6 NSs may improve the penetration of Ce6 in biofilms and further enhance their PDT effect.

The MR imaging ability of MBP-Ce6 NSs in bacterial biofilm microenvironment was further evaluated. As shown in Figure 3(d), the T_1-weighted MR signal of MBP-Ce6 NSs gradually increased in acidic solution (pH = 5.0) with the increase of their concentration, while that in neutral condition (pH = 7.4) showed a much weaker MR signal. Figure 3(e) indicates that the transverse relativity (r_1) of MBP-Ce6 NSs after being incubated in acidic buffer (pH = 5.0) for 24 h is 10.99 $mM^{-1}\,s^{-1}$, which is about 3 times of that in neutral buffer (3.47 $mM^{-1}\,s^{-1}$, pH = 7.4). Such significantly enhanced MR signal proves that MBP-Ce6 NSs could serve as pH-responsive MRI contrast agents.

Then, the efficiency of MBP-Ce6 NSs for the treatment of MRSA biofilms *in vitro* was evaluated. Based on the 3D CLSM images shown in Figure 3(f), MRSA biofilms treated by MBP-Ce6 NSs with both laser irradiation and H_2O_2 have the lowest green fluorescence, indicating their excellent therapeutic effect. In contrast, MRSA biofilms in other groups with different treatments (Ce6 + laser, H_2O_2 + laser, and MBP-Ce6 NSs + laser) showed much stronger fluorescence, suggesting limited antibiofilm effect. The *in vitro* aPDT efficiency of MBP-Ce6 NSs for MRSA biofilms was also studied. As shown in Figure 3(g), the colony-forming units (CFU) number of MRSA biofilms treated by MBP-Ce6 NSs (MnO_2 NSs: 100 μg/mL, Ce6: 80 μg/mL) and H_2O_2 (50 μM) with the laser irradiation decreased by 1.5 log (97%). In comparison, the bacteria inactivation efficiency is less than 0.6 log (75%) for other groups (Ce6 + laser, Ce6 + H_2O_2 + laser, and MBP-Ce6 + laser). For the MBP-Ce6 + H_2O_2 and MBP + H_2O_2 + laser groups, no obvious antibacterial effect can be observed. These results prove that the MBP-Ce6 NSs can achieve excellent antibiofilm performance by aPDT with the presence of H_2O_2, which may be converted into O_2 by the MnO_2 catalyzing and facilitate the generation of $^1O_2$. To verify this assumption, the generation of $^1O_2$ in MRSA biofilms after different treatments was tested. As indicated in Figure S10 (Supporting Information), MRSA biofilms treated by MBP-Ce6 NSs with laser and H_2O_2 showed much stronger fluorescence than those treated by saline, Ce6, and MBP with laser and H_2O_2, suggesting a higher level of $^1O_2$. SEM images (Figure 3(h)) reveal that the MRSA biofilms in MBP-Ce6 + laser + H_2O_2 group show distinctly structure damage, which can also be observed from the images of MRSA biofilms stained by crystal violet with decrease of relative biofilm biomass (Figure S11, Supporting Information).

2.3. Microenvironment-Responsive Dual-Mode Imaging of MRSA Biofilm Infection. In order to evaluate the *in vivo* imaging capability of MBP-Ce6 NSs, MRSA biofilm-infected mice models were constructed by subcutaneously injection of MRSA dispersions into the right thigh (biofilm infected) of each mouse (Figure 4(a)). In comparison, PBS dispersion was also used to treat the left thigh (control) of

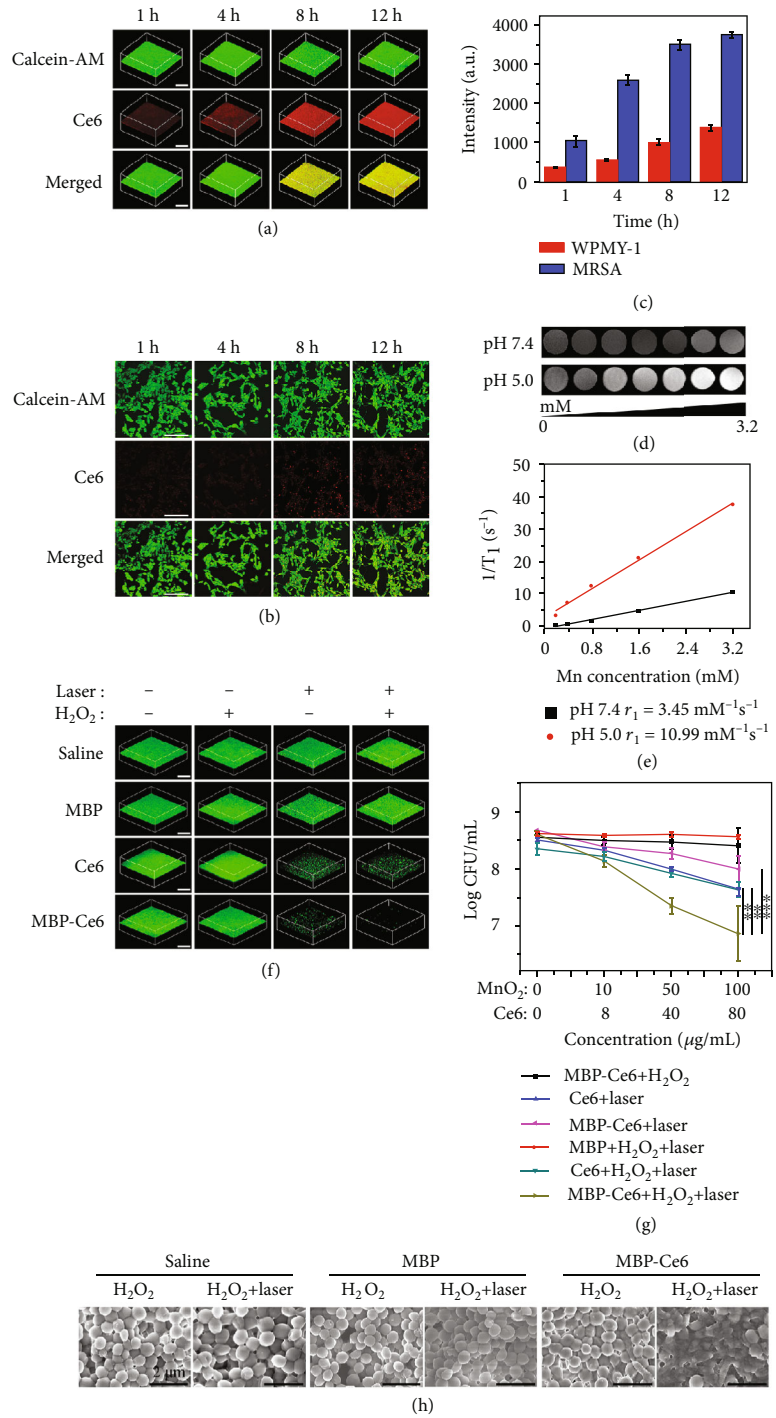


FIGURE 3: *In vitro* Ce6 releasing behavior of MBP-Ce6 NSs and photodynamic treatment of MRSA biofilms. (a) 3D CLSM images of MRSA biofilms after being incubated with MBP-Ce6 (MnO_2 NSs: 100 μg/mL; Ce6: 80 μg/mL) at different times. The scale bar is 200 μm. (b) CLSM images of WPMY-1 cells after being treated with MBP-Ce6 (MnO_2 NSs: 100 μg/mL; Ce6: 80 μg/mL) at different times. The green fluorescence and the red fluorescence originate from Calcein-AM and Ce6, respectively. The scale bar is 200 μm. (c) The fluorescence intensity of Ce6 after MBP-Ce6 NSs (MnO_2 NSs: 100 μg/mL; Ce6: 80 μg/mL) incubated with MRSA biofilms and WPMY-1 cells at different times. (d) T_1-weighted MR images of MBP-Ce6 NSs solutions with different concentrations and pH values in PBS. (e) The transverse relativities (r_1) for MBP-Ce6 NSs under different pH values in PBS. (f) 3D CLSM images of live bacteria (green fluorescence) inside MRSA biofilms after various treatments and stained with Calcein-AM. The scale bar is 200 μm. (g) The CFU number of bacteria inside MRSA biofilms after different treatments. $^{**}p < 0.01$ and $^{***}p < 0.001$ (two-tailed Student's t-test). (h) SEM images of MRSA biofilms treated with saline, MBP NSs (MnO_2 NSs: 100 μg/mL), and MBP-Ce6 NSs (MnO_2 NSs: 100 μg/mL; Ce6: 80 μg/mL) under different conditions. The scale bar is 2 μm. The concentration of H_2O_2 is 50 μM. The laser irradiation was carried out by using the power density of 20 mW/cm^2 at 635 nm for 30 min. Error bars indicate s.d. ($n = 3$).

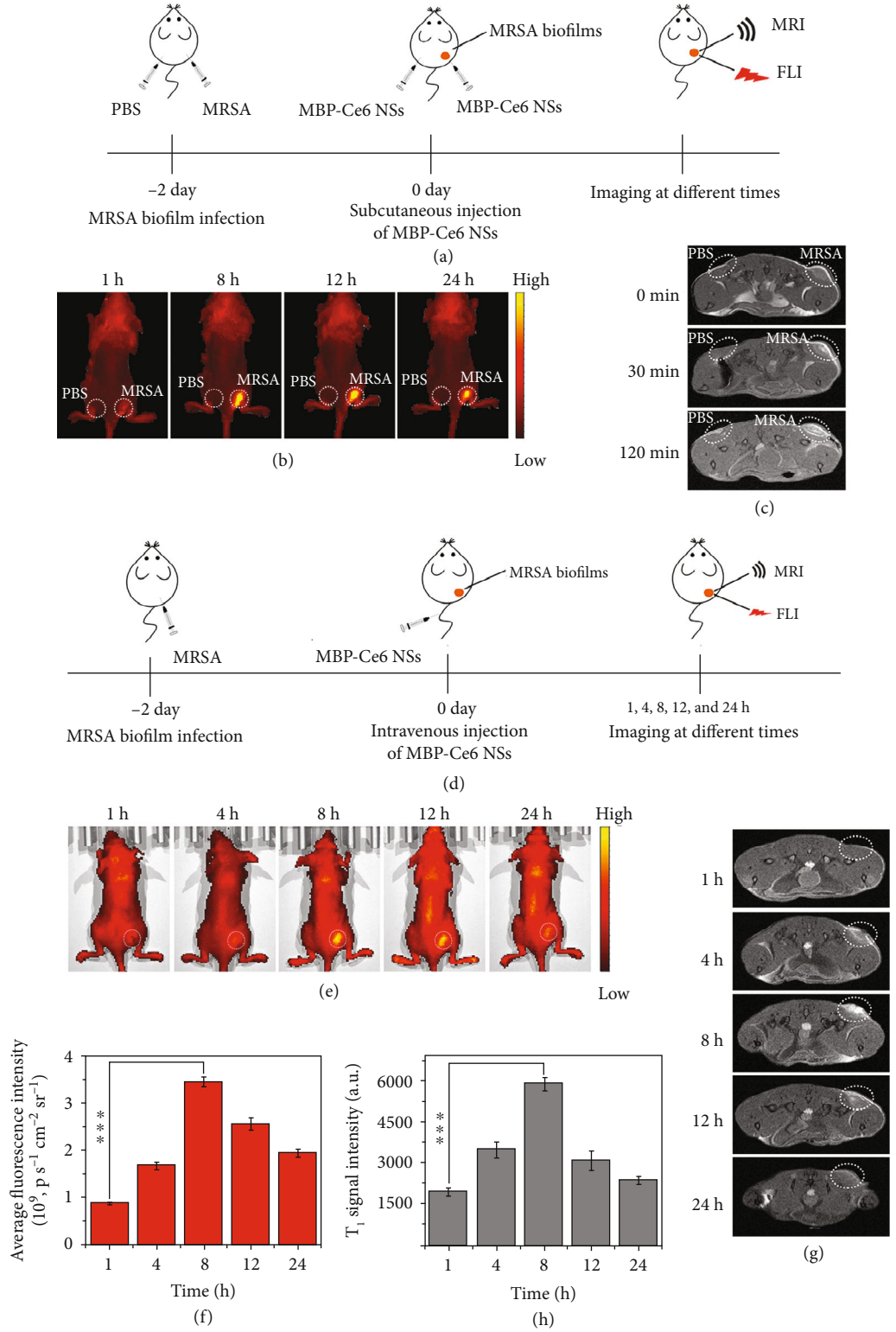


FIGURE 4: *In vivo* fluorescence imaging (FLI) and magnetic resonance imaging (MRI) of MRSA biofilm infections by using MBP-Ce6 NSs. (a) Schematic illustration for the detection of MRSA biofilms by *in situ* injection of MBP-Ce6 NSs (50 μL; MnO_2: 50 μg/mL; and Ce6: 40 μg/mL) both in the left thigh (normal tissue) and the right thigh (infected tissue). (b) Fluorescence images and (c) T_1-weighted MR images of the infected mice at different times. (d) Schematic illustration of the process for the detection of MRSA biofilms by i.v. injection of MBP-Ce6 NSs. (e) Fluorescence images and the (f) fluorescence intensity of MRSA-infected mice at different times postinjection. (g) T_1-weighted MR images shown in cross-section and (h) the intensity of the T_1-weighted MR signal of the MRSA biofilm-infected tissues at different times postinjection. White dashed circles in (e) and (g) denote MRSA biofilm-infected tissues. $^{***}p < 0.001$ (two-tailed Student's t-test). All data are presented as means ± s.d. ($n = 3$).

the same mice. Two days later, MRSA biofilm infections with significant abscesses (Figure S12(a), Supporting Information) appeared and could be confirmed by wound blotting (Figure S12(b), Supporting Information) [55, 56]. The *in vivo* imaging of MRSA biofilms was first studied by *in situ* injection of MBP-Ce6 NSs.

As illustrated in Figure 4(b) and (c), and Figure S13 (Supporting Information), the biofilm-infected tissues (right thigh) showed significantly enhanced fluorescence and T_1-weighted MR signals after local injection of MBP-Ce6 NSs compared with normal tissues (left thigh), which suggests that detection of the MRSA biofilm infections could be achieved by MBP-Ce6 NSs. To further examine the *in vivo* FL/MR dual-mode imaging ability, MBP-Ce6 NSs were used to detect MRSA biofilm infections by intravenous (i.v.) injection (Figure 4(d)). Figure 4(e) and (f) show that the fluorescence of the infected tissues in mice treated by i.v. injection of MBP-Ce6 NSs increased gradually and peaked at the 8th hour postinjection. After 24 h postinjection, the fluorescence signal in biofilm-infected tissues was much stronger than other organs (Figure S14, Supporting Information), indicating specific accumulation in infected tissues due to the EPR effect and pH-responsive decomposition of MBP-Ce6 NSs [29, 42]. Meanwhile, the T_1-weighted MR signal of the MRSA biofilm infections also increased obviously during the first 8 h and gradually decreased afterwards (Figure 4(g) and (h)), similar to the change of fluorescence signal. As Figure S15 (Supporting Information) shows, the T_1-weighted MR signal in the kidneys was much stronger than that in other organs during 24 h postinjection and gradually became weaker after the 8th hour postinjection, suggesting that the Mn^{2+} ions released from MBP-Ce6 NSs could be quickly excreted through the kidney [45]. In addition, we also found that the amount of Mn in biofilm-infected tissues is much higher than that in the other organs, indicating the specific accumulation of MBP-Ce6 NSs in MRSA biofilm-infected tissues (Figure S16, Supporting Information). Furthermore, the content of Mn in the organs quickly decreased to low level within 48 h, which demonstrates that MBP-Ce6 NSs could be quickly excreted from the body after decomposition within relatively short periods [42].

2.4. Relieving Hypoxia for Enhanced PDT of MRSA Biofilm Infection. During the development of bacterial biofilms, O_2 is consumed by both the bacteria inside the biofilms and the surrounding inflammatory cells, while the diffusion of O_2 into the biofilms is hampered by the existence of the dense EPS, which together cause the hypoxia in bacterial biofilm microenvironment [47, 57]. It is known that PDT is an oxygen-dependent process and the therapeutic efficacy can be greatly restricted by the hypoxic conditions. Hence, the hypoxia microenvironment in biofilms is an intrinsic barrier for aPDT treatment. As reported, excess H_2O_2 usually exists in biofilm-infected tissues [4, 28], in principle, which could be converted to O_2 with the catalysis of MnO_2. Herein, the potential of MBP-Ce6 NSs to generate O_2 and relieve the hypoxia of biofilm was investigated in a mice model. After i.v. injection with PBS, Ce6, MBP NSs, and MBP-Ce6 NSs, the biofilm-infected tissues of mice were harvested at 8th hour posttreatment and stained with fluorescent dye-labeled HIF-1α antibody [58].

As shown in Figure 5(a), CLSM images indicate that the MRSA biofilm-infected tissues treated with PBS or Ce6 showed a larger hypoxia-positive area (green), while those treated with MBP NSs or MBP-Ce6 NSs exhibited a limited hypoxia-positive area. The semiquantification analysis results (Figure 5(b)) further confirm that the treatment by MBP NSs or MBP-Ce6 NSs could effectively relieve the hypoxia conditions inside MRSA biofilm-infected tissues. The *in vivo* therapeutic efficacy of aPDT by using MBP-Ce6 NSs was further studied. The mice with MRSA biofilm infections were divided into different groups according to different treatments: laser irradiation (group 1, laser), MBP NSs with laser irradiation (group 2, MBP + L), Ce6 with laser irradiation (group 3, Ce6 + L), MBP-Ce6 NSs (group 4, MBP-Ce6), and MBP-Ce6 NSs with laser irradiation (group 5, MBP-Ce6 + L). After i.v. injection of the agents (dose of MnO_2 = 5 mg/kg; dose of Ce6 = 4 mg/kg) for 8 h, laser irradiation under 635 nm laser (20 mW/cm^2) was performed in groups 1, 2, 3, and 5 for 30 min. At therapeutic day 8, the mice in group 5 (MBP-Ce6 NSs + laser) showed significantly reduction of the infected area compared with the other four groups (Figure 5(c)). The abscesses and wound beds of the mice in group 5 disappeared, while the mice with other treatments (groups 1, 2, 3, and 4) still had a large area of infection (Figure 5(d)). In addition, the infected tissues were harvested and the number of viable bacteria inside biofilm-infected tissues was evaluated at 8th day posttreatment. Figure 5(e) shows that the bacterial inactivation efficiency of group 5 (MBP-Ce6 NSs + laser) is about 2.5 log (99.7%), much higher than those in group 1 (0%), group 2 (0%), group 3 (80.1%), and group 4 (0%). As shown in the hematoxylin-eosin (H&E) staining images (Figure 5(f); Figure S17, Supporting Information), severe inflammation with massive inflammatory cells infiltration still existed in infected tissues of the mice in groups 1-4 (indicated by blue arrows). In contrast, the infected tissues in group 5 (MBP-Ce6 NSs + laser) showed obvious proliferation of fibroblast cells, neovascularization (indicated by green cycles), and a little granulomatous inflammation (indicated by red cycles). Masson's trichrome staining images further indicate the formation of intact subcutaneous tissues and the appearance of more collagen fibers (blue) in group 5 than the other groups (groups 1, 2, 3, and 4), suggesting better recovery of the infected tissues. These results demonstrated that MBP-Ce6 NSs have excellent aPDT efficacy for MRSA biofilm infections, which should be ascribed to the hypoxia-relief in the biofilm microenvironment.

Furthermore, long-term toxicity of MBP-Ce6 NSs to mice was also studied. As shown in Figure S18(a) (Supporting Information), H&E staining images of major organs from the mice after i.v. injection of MBP-Ce6 NSs show no noticeable damage or inflammatory lesion. Figure S18(b) (Supporting Information) indicates that the body weights of the mice treated by MBP-Ce6 NSs steadily increased and had no obvious difference from the mice treated by PBS. The hematology assay results (Figures S19 (c-j), Supporting

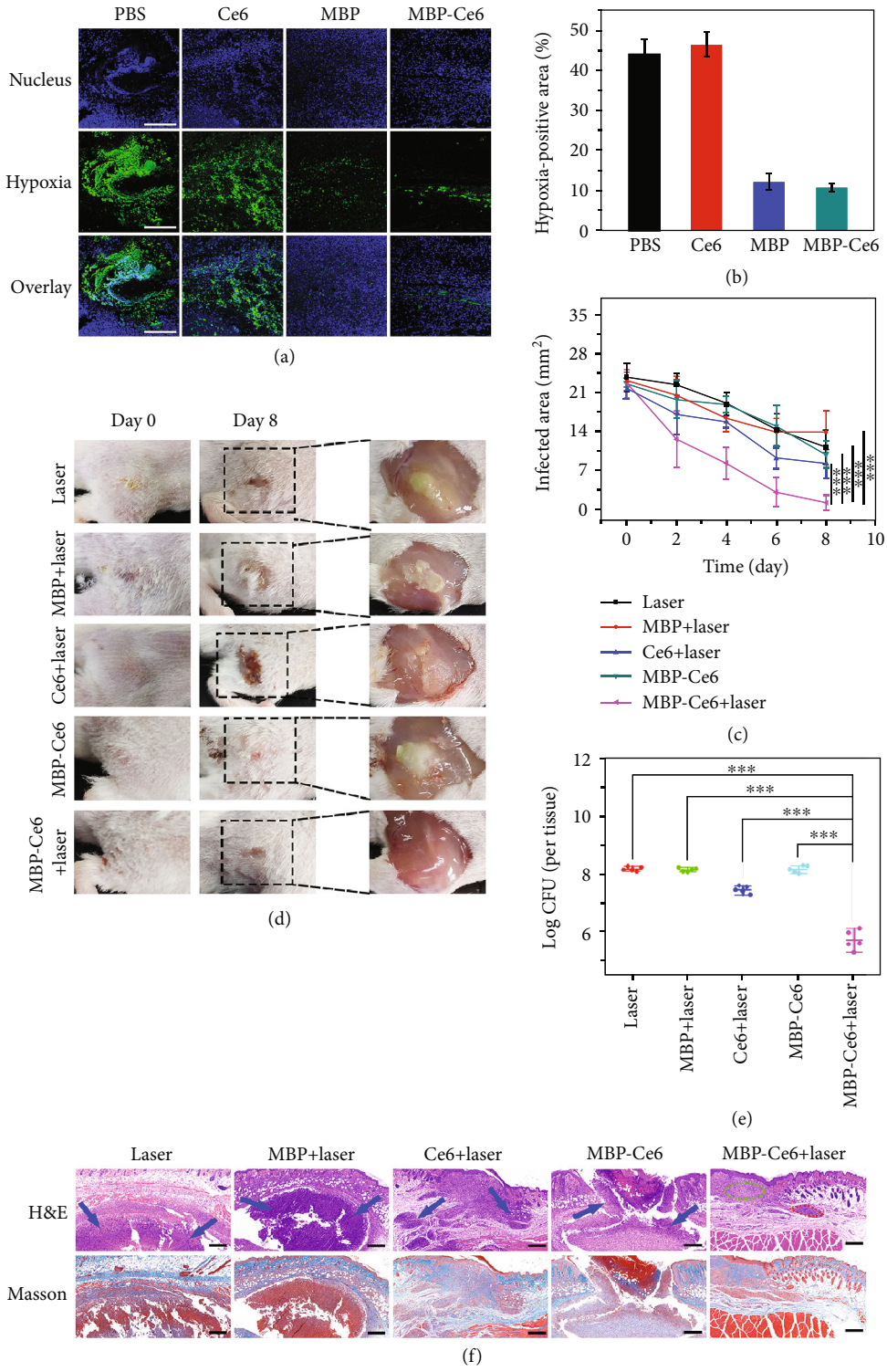


FIGURE 5: Photodynamic treatment of MRSA biofilm infections *in vivo*. (a) CLSM immunofluorescence images of the infected tissue slices from the mice after i.v. injection with PBS, Ce6, MBP NSs, and MBP-Ce6 NSs for 8 h, respectively. The hypoxic condition was indicated by staining the slices with HIF-1α antibody (green) and 4′,6-diamidino-2-phenylindole (DAPI, blue). The scale bar is 200 μm. (b) Semiquantification of the hypoxia-positive area in biofilm-infected tissues after various treatments. (c) Biofilm-infected tissue areas of mice after different treatments at different times. (d) Photographs of the biofilm-infected tissues from the mice with various treatments at different times. (e) CFU of MRSA in biofilm-infected tissues at 8th day posttreatment. (f) Histological analysis of the biofilm-infected tissues by H&E and Masson's trichrome staining. Blue arrows denote the inflammatory cell infiltration. Green circle indicates the proliferation of fibroblast and neovascularization. Red circle indicates granulomatous inflammation. The scale bar is 200 μm. $^{***}p < 0.001$ (two-tailed Student's t-test). All data are presented as means ± s.d. ($n = 5$).

Information) further show that all serum biochemical parameters and blood routine examination parameters of the mice treated by MBP-Ce6 NSs are similar with the control group at 28 d postinjection, further indicating low toxicity of MBP-Ce6 NSs at the dose used in this study [59].

3. Conclusion

In summary, we designed multifunctional nanotheranostics (MBP-Ce6 NSs) for biofilm microenvironment-responsive imaging and treating of MRSA biofilm infections. MBP-Ce6 NSs could be decomposed in the acidic microenvironment in biofilm-infected tissues and subsequently release Ce6 and Mn^{2+} ions. The FL signal from Ce6 and MR signal from Mn^{2+} could be simultaneously activated during the decomposition of MBP-Ce6 NSs. Experimental results show that MBP-Ce6 NSs can achieve FL/MR dual-mode imaging for specific and sensitive detection of MRSA biofilm infections. On the other hand, the hypoxic condition in biofilm microenvironment could be relieved by MnO_2-triggered decomposition of endogenous H_2O_2 in biofilm-infected tissues, while hypoxia-associated resistance of biofilm toward aPDT could be overcome. After being treated by MBP-Ce6 NSs with laser irradiation, the number of viable MRSA from biofilm-infected tissues in mice could be reduced by 2.5 log (99.7%), which is much lower than the control groups, and the recovery of the infected tissues could be promoted. Furthermore, the MBP-Ce6 NSs showed no appreciable toxicity in the *in vivo* study, indicating their potential use in biomedicine. Therefore, this study provides a promising theranostic nanoplatform with potential use for specific detection and treatment of bacterial biofilm infections.

4. Materials and Methods

4.1. Materials. Manganese chloride tetrahydrate ($MnCl_2 \bullet 4H_2O$), tetramethylammonium hydroxide solution (TMA, 1.0 M), bovine serum protein (BSA), and 2′,7′-dichloroflourescin diacetate (DCFH-DA) were purchased from Sigma-Aldrich. NH_2-PEG_{3000} and chlorin e6 (Ce6) were purchased from JenKem Technology and Frontier, respectively. The hydrogen peroxide (H_2O_2, 30 wt.%) solution was purchased from Sinopharm Chemical Reagent Co., Ltd. Dulbecco's modified Eagle's medium (DMEM) and fetal bovine serum (FBS) were bought from KeyGen BioTech and Gibco, respectively. HIF-1α antibody (mouse monoclonal antibody) and FITC-labeled goat anti-mouse IgG were purchased from Beyotime Biotechnology. All solutions were prepared by using ultrapure water (18.2 MΩ).

4.2. Characterization. TEM images were obtained by using an HT7700 transmission electron microscope (Hitachi, Japan). Anatomic force microscope (AFM, Nanoscope IIIa, Bruker, USA) was used to measure the thickness of the nanosheets. X-ray diffraction (XRD) patterns were recorded on a D8 ADVANCE X-ray diffractometer (Bruker, Germany) with Cu Kα radiation. The ultraviolet-visible-infrared (UV-Vis-NIR) absorption spectra were recorded on a UV-3600 spectrophotometer (Shimadzu, Japan). Fluorescence spectra (FL) were recorded on a Shimadzu RF-5301 PC fluorescence spectrophotometer. The concentration of O_2 in solutions was measured by using a dissolved oxygen detection probe (HACH, China). Photodynamic therapy (PDT) was performed by using a 635 nm continuous-wave semiconductor laser (BWT Beijing, China). The power density of laser irradiation was measured by using a digital power meter (PM100D, Thorlabs, USA). Dynamic light scattering (DLS) and zeta potential were performed on a ZetaPALS Potential Analyzer (Brookhaven Instruments, USA).

4.3. Synthesis of MnO_2 NSs. MnO_2 nanosheets (MnO_2 NSs) were prepared based on previous study. Twelve-milliliter TMA solution (0.1 M) and 2 mL H_2O_2 (30 wt.%) were mixed with 6 mL ultrapure water as solution A. $MnCl_2 \bullet 4H_2O$ (0.6 g) was dissolved in 10 mL H_2O as solution B. Then, solution A was quickly mixed with solution B and the color of the mixture became dark brown indicating that the Mn^{2+} was oxidized to Mn^{4+}. After stirring overnight, the aggregated MnO_2 NSs were washed with ethanol and water for three times, respectively, and were then dispersed in 30 mL ultrapure water. To prepare single-layer MnO_2 NSs, the as-prepared MnO_2 aggregations were exfoliated by ultrasonication (Yimaneili, 950 W, 25 kHz) for 10 h in an ice-bath. The mixtures were centrifuged at 12000 rpm for 45 min to separate large aggregations and were further centrifuged at 18000 rpm for 90 min to obtain the single-layer MnO_2 NSs. This step was repeated for three times. The MnO_2 NSs were dispersed in ultrapure water and then stored at 4°C. The concentration of MnO_2 NSs was determined by using an inductively coupled plasma atomic emission spectrometer(ICP-AES, Optima 5300DV, PerkinElmer).

4.4. Preparation of MnO_2-BSA/PEG-Ce6 NSs. MnO_2 NSs (5 mg) and BSA (100 mg) were dispersed in 15 mL water and stirred for 12 h. Then, the mixture was centrifuged at 16000 rpm for 45 min to remove any large aggregations. The MnO_2-BSA nanosheets were dispersed in 15 mL water and mixed with 50 mg PEG_{3000}-NH_2 by stirring for 12 h. The mixture was centrifuged at 16000 rpm for 45 min and washed with water for three times to get MnO_2-BSA/PEG nanosheets (MBP NSs). For Ce6 loading, MBP NSs and Ce6 aqueous dispersions were mixed in an orbital shaker for 12 h and then centrifuged at 16000 rpm for 45 min to obtain MnO_2-BSA/PEG-Ce6 nanosheets (MBP-Ce6 NSs). MBP-Ce6 NSs aqueous dispersions were stored at 4°C.

The loading efficiency and encapsulation efficiency of Ce6 by MBP NSs were determined according to the following equations

$$\text{Ce6 loading efficiency}(\%) = W_1/W_2 \times 100\% \quad (1)$$

$$\text{Ce6 encapsulation efficiency}(\%) = (W_t - W_s)/(W_t) \times 100\% \quad (2)$$

where W_1 is the weight of Ce6 loaded in MBP-Ce6 NSs, W_2 is the total weight of MBP-Ce6 NSs, W_t represents the total weight of Ce6 initially added, and W_s represents the weight of Ce6 remaining in the supernatant.

4.5. Degradation and Drug Release Study of MBP-Ce6 NSs. To study the degradation process, MBP-Ce6 NSs were dispersed in PBS solutions with different pH values (5.0, 6.0, and 7.4). At given time points, the MBP-Ce6 NS PBS dispersions were collected and quantified by using UV-Vis absorption spectra. For Ce6 release studies, the MBP-Ce6 NSs were dispersed in PBS solutions with different conditions (pH 7.4 in PBS, pH 5.0 in PBS, pH 7.4 in PBS with 50 μM H_2O_2, and pH 5.0 in PBS with 50 μM H_2O_2). The amount of released Ce6 was determined by using UV-Vis absorption spectra, and the fluorescence recovery was monitored by using fluorescence spectra.

4.6. Detection of Singlet Oxygen during PDT. 2′, 7′-Dichlorofluorescein diacetate (DCFH-DA) was used to detect the generation of singlet oxygen. In order to detect the photodynamic effect of MBP-Ce6 NSs in hypoxia conditions, O_2 were removed from the PBS solutions by bubbling with N_2 for 30 min. Then, DCFH-DA (10 mg/mL, 5 μL) and Ce6 (1 mg/mL, 10 μL) or MBP-Ce6 (containing 10 μg Ce6) were added into 3 mL PBS solutions either with or without H_2O_2 (50 μM), after being irradiated with a 635 nm laser at the power density of 20 mW/cm^2. The fluorescence spectra of these solutions were collected at different times.

4.7. Cytotoxicity of MnO_2 NSs and MBP-Ce6 NSs. A LDH-Cytotoxicity Colorimetric Assay Kit (BioVision) was used to evaluate the cytotoxicity of MnO_2 NSs and MBP-Ce6 NSs. Human normal prostatic myofibroblast (WPMY-1) cells were cultured in DMEM (Dulbecco's modified Eagle's medium, KeyGen, BioTech) with 10% fetal bovine serum (FBS, Gibco) medium at 37°C under 5% CO_2. WPYM-1 cells were added in 96-well plates with the concentration of 10^4 cell per well. After being cultured for 24 h, the supernatant medium was removed and MnO_2 NS and MBP NS dispersions (200 μL, suspended in DMEM (without FBS)) containing different concentrations of MnO_2 (0, 20, 40, 80, 160, and 320 μg/mL) were added into the 96-well plate. Cells cultured without any nanosheets were set as low control, and those cultured with 1% Triton X-100 were used as high control. After 24 h, 100 μL of supernatant in each well was transferred into another 96-well plate, and 100 μL reaction solution was added into the corresponding well. After 30 min, a microplate reader (PowerWave XS2, BioTek) was used to measure the optical density at 495 nm (OD_{495}). The viability of cells was calculated according to the following formula

$$\text{Cell viability} = 100\% - (A_T - A_L)/(A_H - A_L) \times 100\% \quad (3)$$

where A_T represents the OD_{495} of test sample, A_L represents the OD_{495} of low control, and A_H represents the OD_{495} of high control.

4.8. Bacterial Culture. Methicillin-resistant Staphylococcus aureus (MRSA, ATCC43300) was used in this study. Before being used, a single colony of MRSA was transferred into 5 mL Luria-Bertani (LB) culture and cultured for 10 h. The bacterial dispersion was washed with saline and quantitated by a microplate reader. To obtain mature MRSA biofilms, MRSA dispersion in LB culture (containing 1% glucose, 10^7 CFU/mL) was cultured at 37°C for 48 h.

4.9. Ce6 Release in MRSA Biofilms. For pH-responsive Ce6 release study, MRSA biofilms were cultured in a confocal petri dish. The MBP NSs (MnO_2: 100 μg/mL; Ce6: 80 μg/mL) were cultured with MRSA biofilms at 37°C at different times (1, 4, 8, and 12 h). After being washed with saline for three times, MRSA biofilms were stained with Calcein-AM (KeyGen BioTech) for 30 min and then imaged by an Olympus IX81 confocal laser scanning microscope. The 3D images were obtained by using the FV10-ASW Viewer.

4.10. In Vitro Photodynamic Treatment of MRSA Biofilms. To treat the MRSA biofilms by PDT, MBP NSs (MnO_2: 10, 50, and 100 μg/mL) and MBP-Ce6 NSs (MnO_2: 10, 50, and 100 μg/mL and Ce6: 8, 40, and 80 μg/mL) were added into MRSA biofilms with or without H_2O_2 (50 μM). After being cultured for 12 h, the MRSA biofilms in the laser treatment groups were irradiated with 635 nm laser (20 mW/cm^2). MRSA biofilms after different treatments were harvested by ultrasonication. The standard plate count method was used to determine the number of viable bacteria inside MRSA biofilms.

For fluorescence imaging, the treated MRSA biofilms were stained with Calcein-AM for 30 min and imaged by using a confocal laser scanning microscope (Olympus IX81). For crystal violet staining, MRSA biofilms were fixed with formalin for 10 min and dyed with crystal violet solution (0.02%) for 1 h. Images were captured by using a motorized fluorescence microscope (Olympus IX71). For SEM imaging, MRSA biofilms were grown on the surface of an indium tin oxide (ITO) glass. After treatment, MRSA biofilms were fixed in 2.5% glutaraldehyde solution for 30 min, dehydrated with series of ethanol solutions with gradient concentrations (15%, 30%, 50%, 75%, and 100%) for 15 min, respectively. After sputtering coated with gold, the morphology characterization of bacteria was performed on a Hitachi S4800 SEM.

4.11. MRSA Biofilm-Infected Animal Models. All animal procedures were performed in accordance with the Guidelines for Care and Use of Laboratory Animals, and experiments were approved by the Animal Ethics Committee of Nanjing University. Female Balb/c mice (20 g, 6 weeks old) were purchased from Nanjing Junke Biological Engineering Co., Ltd and used in this study. To develop the MRSA biofilm-infected mice model, MRSA suspensions in PBS (50 μL, 10^9 CFU/mL) were subcutaneously injected into the mice skin. After being infected for 2 days, subcutaneous abscesses appeared in the treated mice, indicating the formation of MRSA biofilms.

4.12. FL and MR Imaging of MRSA Biofilm-Infected Mice. Before the FL and MR imaging, MBP-Ce6 NSs dispersions were intravenously (i.v.) injected into MRSA-infected mice (dose of MnO_2 = 5 mg/kg, dose of Ce6 = 4 mg/kg). Fluorescence images of mice at different times (1 h, 4 h, 8 h, 12 h, and 24 h) postinjection were captured on an IVIS Lumina K Series III system (Perkin Elmer). MR imaging was conducted on a MRI scanner system (BioSpec 7T/20 USR,

Bruker) at different times (1 h, 4 h, 8 h, 12 h, and 24 h) postinjection of MBP-Ce6 NSs. The MRI images were obtained by using the Sante MRI Viewer.

4.13. Photodynamic Therapy of MRSA Biofilm-Infected Mice. Thirty mice with MRSA biofilm infections were randomly divided into five groups: (1) saline + laser, (2) MBP NSs + laser, (3) Ce6 + laser, (4) MBP-Ce6 NSs, and (5) MBP-Ce6 NSs + laser. The mice in groups 1-3 were i.v. injected with saline (200 μL), MBP NS dispersion in PBS (200 μL; MnO_2: 5 mg/kg), Ce6 dispersion in PBS (200 μL; dose of Ce6: 4 mg/kg), respectively. The mice in groups 4 and 5 were i.v. injected with MBP-Ce6 NSs dispersions (200 μL; MnO_2: 5 mg/kg, Ce6: 4 mg/kg). At 8th hour postinjection, the mice in the laser treatment groups (groups 1, 2, 3, and 5) were irradiated with 635 nm laser at the power density of 20 mW/cm^2 for 30 min. The size of the infected tissues was measured by using caliper every 2 days. The area of the infected tissues was calculated according to the formula: area = $(\text{width}/2 \times \text{length}/2) \times \pi$. After the treatment for 8 days, the infected tissues of the mice were harvested and ultrasonicated for 10 min to disperse the bacteria. Then, the CFU numbers of the bacteria in the infected tissues were determined by the plate count method.

For histological analysis, the infected tissues of mice were harvested and fixed with 4% polyoxymethylene and then processed by standard protocols for hematoxylin and eosin (H&E) staining and Masson's trichrome staining, respectively.

4.14. Immunofluorescence Staining of MRSA Biofilm-Infected Tissues. MRSA biofilm-infected mice were i.v. injected with saline (200 μL), Ce6 (200 μL, 4 mg/kg), MBP NSs (200 μL, MnO_2: 5 mg/kg), and MBP-Ce6 NSs (200 μL, MnO_2: 5 mg/kg, Ce6: 4 mg/kg), respectively. At 8th hour postinjection, the infected tissues of mice were harvested, fixed with 4% polyoxymethylene, embedded in paraffin, and sectioned into slices. Triton X-100 solution (0.5%) was used for cell lysis. BSA was used to prevent nonspecific adsorption. The tissue slices were incubated with HIF-1α mouse monoclonal antibody at 4°C overnight. Then, the FITC-labeled goat anti-mouse secondary antibody was added at 37°C for 2 h. Cell nuclei were stained with 4′,6-diamidino-2-phenylindole (DAPI). Fluorescence images of the stained tissue slices were obtained by using the confocal laser scanning microscope (Olympus IX81).

4.15. Toxicity Study of MBP-Ce6 NSs In Vivo. Twelve Balb/c mice were randomly divided into two groups (6 mice per group) and were i.v. injected with 200 μL PBS (group a) and 200 μL MBP-Ce6 NSs (group b; MnO_2: 10 mg/kg, Ce6: 8 mg/kg), respectively. At 28th day postinjection, one mouse was sacrificed to afford the major organs (heart, liver, spleen, lung, and kidney) for H&E staining. The blood of the other five mice was collected for hematology assay. For the blood chemistry analysis, the levels of alkaline phosphatase (ALP), alanine aminotransferase (ALT), aspartate aminotransferase (AST), and urea nitrogen (BUN) were measured. For the complete blood panel test, the levels of white blood cells (WBC), red blood cells (RBC), platelets (PLT), hemoglobin (Hgb), hematocrit (HCT), mean corpuscular volume (MCV), mean corpuscular hemoglobin concentration (MCHC), and mean corpuscular hemoglobin (MCH) were measured.

Data Availability

All data needed to evaluate the conclusions in the paper are present in the paper. Additional data related to this paper may be requested from the authors.

Conflicts of Interest

The authors declare no competing financial interest.

Authors' Contributions

L. Wang and L. Yuwen conceived the idea and supervised the study. W. Xiu carried out the experiments, analyzed the results, and wrote the manuscript. S. Gan helped with the *in vivo* experiments. Q. Wen, Q. Qiu, and S. Dai contributed to the material characterization and data analysis. H. Dong, Q. Li, and Y. Mou analyzed the H&E-stained slices. L. Weng and Z. Teng contributed to the scientific discussion of the manuscript. All authors discussed the results and participated in revising the paper.

Acknowledgments

This work was financially supported by the National Key Research and Development Program of China (2017YFA0205302), Natural Science Foundation of Jiangsu Province (BK20191382), the Priority Academic Program Development of Jiangsu Higher Education Institutions (PAPD, YX030003), the Jiangsu Provincial Key Research and Development Program (BE2018732), and the Natural Science Key Fund for Colleges and Universities in Jiangsu Province (17KJA430011).

Supplementary Materials

Figure S1: TEM image of the as-prepared MnO_2 NSs aggregations. Figure S2: large-scale TEM images and size statistics of MnO_2 NSs, MBP NSs, and MBP-Ce6 NSs. Figure S3: selected area electron diffraction pattern and elemental mapping images of MnO_2 NSs. Figure S4: large-scale AFM images and thickness statistics of MnO_2 NSs, MBP NSs, and MBP-Ce6 NSs. Figure S5: hydrodynamic diameter and zeta potential of MnO_2 NSs, MBP NSs, and MBP-Ce6 NSs. Figure S6: fluorescence recovery of MBP-Ce6 NSs at different conditions. Figure S7: the generation of singlet oxygen by MBP-Ce6 NSs. Figure S8: the colloidal stability characterization of MBP-Ce6 NSs. Figure S9: the cytotoxicity of MBP-Ce6 NSs. Figure S10: the ROS in MRSA biofilms treated by MBP-Ce6 NSs and H_2O_2. Figure S11: the crystal violet staining images of MRSA biofilms after photodynamic treatment. Figure S12: photographs of MRSA biofilm-infected tissues and nitrocellulose membrane contacted with the infected issues and followed by ruthenium red staining. Figure S13:

the quantitative data of the FL and MRI imaging for the biofilm-infected mice. Figure S14: fluorescence images of the major organs and MRSA biofilm-infected tissues from the mice treated by MBP-Ce6 NSs. Figure S15: T_1-weighted MR images of the mice in longitudinal section after i.v. injection of MBP-Ce6 NSs. Figure S16: biodistribution of Mn in major organs and MRSA biofilm-infected tissues from the mice treated by MBP-Ce6 NSs. Figure S17: analysis of H&E-stained slices of MRSA-infected tissues from mice. Figure S18: the *in vivo* toxicity evaluation of MBP-Ce6 NSs. *(Supplementary Materials)*

References

[1] L. Hall-Stoodley, J. W. Costerton, and P. Stoodley, "Bacterial biofilms: from the natural environment to infectious diseases," *Nature Reviews Microbiology*, vol. 2, no. 2, pp. 95–108, 2004.

[2] Z. Chen, H. Ji, C. Liu, W. Bing, Z. Wang, and X. Qu, "A multinuclear metal complex based DNase-mimetic artificial enzyme: matrix cleavage for combating bacterial biofilms," *Angewandte Chemie International Edition*, vol. 55, no. 36, pp. 10732–10736, 2016.

[3] D. Davies, "Understanding biofilm resistance to antibacterial agents," *Nature Reviews Drug Discovery*, vol. 2, no. 2, pp. 114–122, 2003.

[4] Q. Deng, P. Sun, L. Zhang et al., "Porphyrin MOF dots–based, function-adaptive nanoplatform for enhanced penetration and photodynamic eradication of bacterial biofilms," *Advanced Functional Materials*, vol. 29, no. 30, article 1903018, 2019.

[5] K. Lewis, "Persister cells, dormancy and infectious disease," *Nature Reviews Microbiology*, vol. 5, no. 1, pp. 48–56, 2007.

[6] H. C. Flemming, J. Wingender, U. Szewzyk, P. Steinberg, S. A. Rice, and S. Kjelleberg, "Biofilms: an emergent form of bacterial life," *Nature Reviews Microbiology*, vol. 14, no. 9, pp. 563–575, 2016.

[7] H. Wu, C. Moser, H. Z. Wang, N. Høiby, and Z. J. Song, "Strategies for combating bacterial biofilm infections," *International Journal of Oral Science*, vol. 7, no. 1, pp. 1–7, 2015.

[8] B. P. Conlon, E. S. Nakayasu, L. E. Fleck et al., "Activated ClpP kills persisters and eradicates a chronic biofilm infection," *Nature*, vol. 503, no. 7476, pp. 365–370, 2013.

[9] A. Penesyan, M. Gillings, and I. Paulsen, "Antibiotic discovery: combatting bacterial resistance in cells and in biofilm communities," *Molecules*, vol. 20, no. 4, pp. 5286–5298, 2015.

[10] G. Fang, W. Li, X. Shen et al., "Differential Pd-nanocrystal facets demonstrate distinct antibacterial activity against Gram-positive and Gram-negative bacteria," *Nature Communications*, vol. 9, no. 1, article 129, 2018.

[11] X. Ning, W. Seo, S. Lee et al., "PET imaging of bacterial infections with fluorine-18-labeled maltohexaose," *Angewandte Chemie International Edition*, vol. 53, no. 51, pp. 14096–14101, 2014.

[12] D. K. Kang, M. M. Ali, K. Zhang et al., "Rapid detection of single bacteria in unprocessed blood using integrated comprehensive droplet digital detection," *Nature Communications*, vol. 5, no. 1, article 5427, 2014.

[13] L. Hall-Stoodley, F. Z. Hu, A. Gieseke et al., "Direct detection of bacterial biofilms on the middle-ear mucosa of children with chronic otitis media," *JAMA*, vol. 296, no. 2, pp. 202–211, 2006.

[14] M. K. S. Larsen, T. R. Thomsen, C. Moser, N. Høiby, and P. H. Nielsen, "Use of cultivation-dependent and -independent techniques to assess contamination of central venous catheters: a pilot study," *BMC Clinical Pathology*, vol. 8, no. 1, p. 10, 2008.

[15] J. Tang, B. Chu, J. Wang et al., "Multifunctional nanoagents for ultrasensitive imaging and photoactive killing of Gram-negative and Gram-positive bacteria," *Nature Communications*, vol. 10, no. 1, article 4057, 2019.

[16] Z. Zhao, R. Yan, X. Yi et al., "Bacteria-activated theranostic nanoprobes against methicillin-resistant *Staphylococcus aureus* infection," *ACS Nano*, vol. 11, no. 5, pp. 4428–4438, 2017.

[17] X. Ning, S. Lee, Z. Wang et al., "Maltodextrin-based imaging probes detect bacteria *in vivo* with high sensitivity and specificity," *Nature Materials*, vol. 10, no. 8, pp. 602–607, 2011.

[18] M. van Oosten, T. Schäfer, J. A. C. Gazendam et al., "Real-time *in vivo* imaging of invasive- and biomaterial-associated bacterial infections using fluorescently labelled vancomycin," *Nature Communications*, vol. 4, no. 1, article 2584, 2013.

[19] K. E. DeMeester, H. Liang, M. R. Jensen et al., "Synthesis of functionalized *N*-acetyl muramic acids to probe bacterial cell wall recycling and biosynthesis," *Journal of the American Chemical Society*, vol. 140, no. 30, pp. 9458–9465, 2018.

[20] Z. Zhao, H. Fan, G. Zhou et al., "Activatable fluorescence/MRI bimodal platform for tumor cell imaging via MnO_2 nanosheet–aptamer nanoprobe," *Journal of the American Chemical Society*, vol. 136, no. 32, pp. 11220–11223, 2014.

[21] S. Zhu, R. Tian, A. L. Antaris, X. Chen, and H. Dai, "Near-infrared-II molecular dyes for cancer imaging and surgery," *Advanced Materials*, vol. 31, no. 24, article 1900321, 2019.

[22] E. Terreno, D. D. Castelli, A. Viale, and S. Aime, "Challenges for molecular magnetic resonance imaging," *Chemical Reviews*, vol. 110, no. 5, pp. 3019–3042, 2010.

[23] X. Pang, X. Liu, Y. Cheng et al., "Sono-immunotherapeutic nanocapturer to combat multidrug-resistant bacterial infections," *Advanced Materials*, vol. 31, no. 35, article 1902530, 2019.

[24] A. Gupta, R. Das, G. Yesilbag Tonga, T. Mizuhara, and V. M. Rotello, "Charge-switchable nanozymes for bioorthogonal imaging of biofilm-associated infections," *ACS Nano*, vol. 12, no. 1, pp. 89–94, 2018.

[25] T. F. Moriarty, J. S. Elborn, and M. M. Tunney, "Effect of pH on the antimicrobial susceptibility of planktonic and biofilm-grown clinical *Pseudomonas aeruginosa* isolates," *British Journal of Biomedical Science*, vol. 64, no. 3, pp. 101–104, 2007.

[26] P. O. Jensen, M. Kolpen, K. N. Kragh, and M. Kuhl, "Microenvironmental characteristics and physiology of biofilms in chronic infections of CF patients are strongly affected by the host immune response," *APMIS*, vol. 125, no. 4, pp. 276–288, 2017.

[27] Y. Liu, Z. Ren, G. Hwang, and H. Koo, "Therapeutic strategies targeting cariogenic biofilm microenvironment," *Advances in Dental Research*, vol. 29, no. 1, pp. 86–92, 2018.

[28] D. Mao, F. Hu, Kenry et al., "Metal-organic-framework-assisted *in vivo* bacterial metabolic labeling and precise antibacterial therapy," *Advanced Materials*, vol. 30, no. 18, article 1706831, 2018.

[29] D. S. Benoit and H. Koo, "Targeted, triggered drug delivery to tumor and biofilm microenvironments," *Nanomedicine*, vol. 11, no. 8, pp. 873–879, 2016.

[30] D. S. W. Benoit, K. R. Sims Jr., and D. Fraser, "Nanoparticles for oral biofilm treatments," *ACS Nano*, vol. 13, no. 5, pp. 4869–4875, 2019.

[31] Z. Xu, Z. Qiu, Q. Liu et al., "Converting organosulfur compounds to inorganic polysulfides against resistant bacterial infections," *Nature Communications*, vol. 9, no. 1, article 3713, 2018.

[32] Y. Liu, H. C. van der Mei, B. Zhao et al., "Eradication of Multidrug-Resistant *Staphylococcal* Infections by light-activatable micellar nanocarriers in a murine model," *Advanced Functional Materials*, vol. 27, no. 44, article 1701974, 2017.

[33] D. Hu, H. Li, B. Wang et al., "Surface-adaptive gold nanoparticles with effective adherence and enhanced photothermal ablation of methicillin-resistant *Staphylococcus aureus* biofilm," *ACS Nano*, vol. 11, no. 9, pp. 9330–9339, 2017.

[34] H. Zhu, Y. Fang, Q. Miao et al., "Regulating near-infrared photodynamic properties of semiconducting polymer nanotheranostics for optimized cancer therapy," *ACS Nano*, vol. 11, no. 9, pp. 8998–9009, 2017.

[35] H. Zhu, J. Li, X. Qi, P. Chen, and K. Pu, "Oxygenic Hybrid semiconducting nanoparticles for enhanced photodynamic therapy," *Nano Letters*, vol. 18, no. 1, pp. 586–594, 2018.

[36] D. Xu, C. Zhou, C. Zhan et al., "Enzymatic micromotors as a mobile photosensitizer platform for highly efficient on-chip targeted antibacteria photodynamic therapy," *Advanced Functional Materials*, vol. 29, no. 17, article 1807727, 2019.

[37] K. Kai, Y. Yoshida, H. Kageyama et al., "Room-temperature synthesis of manganese oxide monosheets," *Journal of the American Chemical Society*, vol. 130, no. 47, pp. 15938–15943, 2008.

[38] Y. Chen, D. Ye, M. Wu et al., "Break-up of two-dimensional MnO_2 nanosheets promotes ultrasensitive pH-triggered theranostics of cancer," *Advanced Materials*, vol. 26, no. 41, pp. 7019–7026, 2014.

[39] D. He, X. He, K. Wang et al., "Redox-responsive degradable honeycomb manganese oxide nanostructures as effective nanocarriers for intracellular glutathione-triggered drug release," *Chemical Communications*, vol. 51, no. 4, pp. 776–779, 2015.

[40] Y. Zhang, W. Xiu, Y. Sun et al., "RGD-QD-MoS_2 nanosheets for targeted fluorescent imaging and photothermal therapy of cancer," *Nanoscale*, vol. 9, no. 41, pp. 15835–15845, 2017.

[41] L. Zhao, H. Yang, T. Amano et al., "Efficient delivery of chlorin e6 into ovarian cancer cells with octalysine conjugated superparamagnetic iron oxide nanoparticles for effective photodynamic therapy," *Journal of Materials Chemistry B*, vol. 4, no. 47, pp. 7741–7748, 2016.

[42] Q. Chen, L. Feng, J. Liu et al., "Intelligent Albumin-MnO_2 Nanoparticles as pH-/H_2O_2-Responsive dissociable nanocarriers to modulate tumor hypoxia for effective combination therapy," *Advanced Materials*, vol. 28, no. 33, pp. 7129–7136, 2016.

[43] W. Fan, W. Bu, B. Shen et al., "Intelligent MnO_2 nanosheets anchored with upconversion nanoprobes for concurrent pH/H_2O_2-responsive UCL imaging and oxygen-elevated synergetic therapy," *Advanced Materials*, vol. 27, no. 28, pp. 4155–4161, 2015.

[44] S. Lin, H. Cheng, Q. Ouyang, and H. Wei, "Deciphering the quenching mechanism of 2D MnO_2 nanosheets towards Au nanocluster fluorescence to design effective glutathione biosensors," *Analytical Methods*, vol. 8, no. 19, pp. 3935–3940, 2016.

[45] G. Yang, L. Xu, Y. Chao et al., "Hollow MnO_2 as a tumor-microenvironment-responsive biodegradable nano-platform for combination therapy favoring antitumor immune responses," *Nature Communications*, vol. 8, no. 1, article 902, 2017.

[46] X. Wang, D. Niu, Q. Wu et al., "Iron oxide/manganese oxide co-loaded hybrid nanogels as pH-responsive magnetic resonance contrast agents," *Biomaterials*, vol. 53, pp. 349–357, 2015.

[47] P. S. Stewart and M. J. Franklin, "Physiological heterogeneity in biofilms," *Nature Reviews Microbiology*, vol. 6, no. 3, pp. 199–210, 2008.

[48] Y. K. Wu, N. C. Cheng, and C. M. Cheng, "Biofilms in chronic wounds: pathogenesis and diagnosis," *Trends in Biotechnology*, vol. 37, no. 5, pp. 505–517, 2019.

[49] K. Mathee, O. Ciofu, C. Sternberg et al., "Mucoid conversion of Pseudomonas aeruginos by hydrogen peroxide: a mechanism for virulence activation in the cystic fibrosis lung," *Microbiology*, vol. 145, no. 6, pp. 1349–1357, 1999.

[50] C. Nathan and A. Cunningham-Bussel, "Beyond oxidative stress: an immunologist's guide to reactive oxygen species," *Nature Reviews Immunology*, vol. 13, no. 5, pp. 349–361, 2013.

[51] Q. Chen, C. Liang, X. Sun et al., "H_2O_2-responsive liposomal nanoprobe for photoacoustic inflammation imaging and tumor theranostics via in vivo chromogenic assay," *Proceedings of the National Academy of Sciences of the United States of America*, vol. 114, no. 21, pp. 5343–5348, 2017.

[52] J. X. Fan, M. Y. Peng, H. Wang et al., "Engineered bacterial bioreactor for tumor therapy via Fenton-like reaction with localized H_2O_2 Generation," *Advanced Materials*, vol. 31, no. 16, article 1808278, 2019.

[53] Y. Jiang, J. Li, Z. Zeng, C. Xie, Y. Lyu, and K. Pu, "Organic photodynamic nanoinhibitor for synergistic cancer therapy," *Angewandte Chemie International Edition*, vol. 58, no. 24, pp. 8161–8165, 2019.

[54] Q. Miao and K. Pu, "Organic semiconducting agents for deep-tissue molecular imaging: second near-infrared fluorescence, self-luminescence, and photoacoustics," *Advanced Materials*, vol. 30, no. 49, article 1801778, 2018.

[55] S. L. Percival, K. E. Hill, D. W. Williams, S. J. Hooper, D. W. Thomas, and J. W. Costerton, "A review of the scientific evidence for biofilms in wounds," *Wound Repair and Regeneration*, vol. 20, no. 5, pp. 647–657, 2012.

[56] G. Nakagami, G. Schultz, D. J. Gibson et al., "Biofilm detection by wound blotting can predict slough development in pressure ulcers: a prospective observational study," *Wound Repair and Regeneration*, vol. 25, no. 1, pp. 131–138, 2017.

[57] M. Sønderholm, T. Bjarnsholt, M. Alhede et al., "The consequences of being in an infectious biofilm: microenvironmental conditions governing antibiotic tolerance," *International Journal of Molecular Sciences*, vol. 18, no. 12, pp. 2688–2701, 2017.

[58] Z. Wang, Y. Zhang, E. Ju et al., "Biomimetic nanoflowers by self-assembly of nanozymes to induce intracellular oxidative damage against hypoxic tumors," *Nature Communications*, vol. 9, no. 1, article 3334, 2018.

[59] J. Hao, G. Song, T. Liu et al., "In Vivo long-term biodistribution, excretion, and toxicology of PEGylated transition-metal dichalcogenides MS_2 (M = Mo, W, Ti) nanosheets," *Advanced Science*, vol. 4, no. 1, article 1600160, 2017.